Advances in Aerospace Science and Technology, 2026, 11(3), 77-95
https://www.scirp.org/journal/aast
ISSN Online: 2473-6724
ISSN Print: 2473-6708

Trajectory Optimisation and Manoeuvrability Trade-Offs for Hypersonic Glide Vehicles in Contested Atmospheric Re-Entry

Ruggero Doronzo

Independent Researcher, Foggia, Italy
Email: Ruggero.doronzo@me.com

How to cite this paper: Doronzo, R. (2026) Trajectory Optimisation and Manoeuvrability Trade-Offs for Hypersonic Glide Vehicles in Contested Atmospheric Re-Entry. *Advances in Aerospace Science and Technology*, **11**, 77-95.
https://doi.org/10.4236/aast.2026.113005

Received: May 9, 2026
Accepted: July 27, 2026
Published: July 30, 2026

Abstract

Hypersonic Glide Vehicles (HGVs) have become the focal point of a renewed great-power competition in long-range strike capability. Unlike traditional ballistic re-entry vehicles, HGVs spend the majority of their flight in the upper atmosphere at Mach numbers between 5 and 25, executing manoeuvres that render conventional missile defence architectures largely ineffective. This paper develops an analytical and simulation-based framework for HGV trajectory optimisation under realistic atmospheric and structural constraints, with explicit attention to the manoeuvrability-range-survivability trade space. Three reference trajectories are presented and compared: ballistic, equilibrium glide, and skip-glide. Bank-angle modulation produces lateral displacements of +/−800 km without violating thermal protection or load-factor constraints, and the resulting tracking degradation against legacy SAM systems exceeds 60% under conservative assumptions. The framework is grounded in Sutton-Graves stagnation heating correlations, a standard exponential atmosphere, and Newtonian aerodynamic theory, making it fully reproducible from open-source tools.

Keywords

Hypersonic Glide Vehicle, Atmospheric Re-Entry, Trajectory Optimisation, Manoeuvrability, Missile Defence, Bank-Angle Modulation, Sutton-Graves Heating, Cross-Range Capability, Skip-Glide

1. Introduction

Hypersonic atmospheric flight has been demonstrated since the 1960s. The Apollo command module re-entered the atmosphere at roughly Mach 32 in 1969, and the

Space Shuttle did so routinely at Mach 25 for three decades. The distinguishing feature and what has triggered the current strategic concern among major space-faring nations is the prospect of maneuvering at hypersonic speeds for sustained periods, while remaining inside the atmosphere, with sufficient lift-to-drag ratio to defeat conventional missile-defense sensors and interceptors. The Hypersonic Glide Vehicle (HGV) represents the practical implementation of this concept.

DARPA's HTV-2 programme conducted two test flights in 2010 and 2011, both of which ended prematurely but demonstrated that lifting re-entry from boost-glide trajectories is feasible at Mach 20-class speeds [1]. Russia has publicly fielded the Avangard system on its UR-100N rocket booster [1], claiming intercontinental range and Mach 20+ terminal speeds. China has tested the DF-ZF (also reported as WU-) repeatedly since 2014 [1]. Although these programmes are not fully disclosed, the open scientific literature contains sufficient information to develop credible engineering analyses, which constitutes the objective of the present study.

The technical question driving this work is straightforward to state and surprisingly subtle to answer: given a fixed re-entry insertion condition, what trajectory should an HGV follow to maximise the probability of reaching its target? Range alone is not the answer. A purely ballistic re-entry maximises range trivially but is also trivially predictable. A pure equilibrium glide trajectory minimises heating but stays within a narrow band that early-warning radars can pre-cue. What HGV designers actually appear to be doing is deliberately giving up some kinetic energy to gain manoeuvrability, then exploiting that manoeuvrability to make the trajectory unpredictable enough to defeat the defender's decision cycle.

The paper is organised as follows. Section 2 reviews the physics of hypersonic flight and presents the equations of motion. Section 3 surveys HGV aerodynamic configurations. Section 4 formulates the trajectory optimisation constraints. Section 5 simulates three reference trajectories. Section 6 treats lateral manoeuvring through bank-angle modulation. Section 7 examines the implications for missile defence. Section 8 concludes.

2. The Hypersonic Flight Regime

2.1. Defining Hypersonic

The boundary between supersonic and hypersonic flow is not sharp. Anderson places it conventionally at $M = 5$, but a more physically precise characterisation is qualitative: the regime in which linearised theories of compressible flow break down, real-gas effects (vibrational excitation, dissociation, ionisation) begin to matter, and viscous interaction with the inviscid outer flow becomes strong. By $M = 8$ all of these effects are firmly active. By $M = 15$ the air behind a normal shock is partially ionised.

Figure 1 shows the operational corridor in the altitude-velocity plane along with the principal physical constraints: stagnation heat flux, dynamic pressure, and Mach isolines. The shaded green region is within which HGV operations are physically constrained: high enough to keep heat flux manageable, low enough to retain aerodynamic control authority, fast enough to compress decision timelines for any defender.

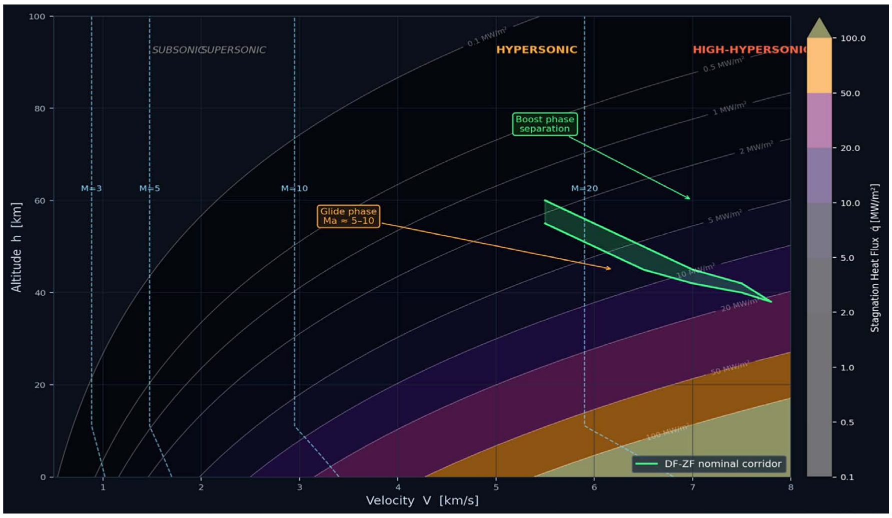

Figure 1. Hypersonic flight regime in the altitude-velocity plane. The hot-coloured background shows stagnation-point heat flux from the Sutton-Graves correlation. Dashed red lines mark TPS-relevant heat flux limits; dotted cyan lines mark dynamic pressure constraints; grey lines are Mach isolines. The shaded green corridor is the typical HGV operating envelope.

2.2. Equations of Motion

For trajectory analysis we use a non-rotating spherical Earth and treat the vehicle as a point mass with controllable bank angle. This approach loses Coriolis effects and the second-order influence of Earth oblateness, both of which matter at the few-percent level but neither of which changes the qualitative findings of this study. The state vector is $(V, \gamma, h, \theta, \psi, \varphi)$ where V is speed, γ is the flight path angle, h is altitude, θ is downrange angle, ψ is heading, and φ is cross-range angle. The four governing equations in the longitudinal plane are:

$$\frac{\mathrm{d}V}{\mathrm{d}t} = -\frac{D}{m} - g\sin\gamma \tag{1}$$

$$\frac{\mathrm{d}\gamma}{\mathrm{d}t} = \left[\frac{L\cos\sigma}{mV}\right] - \left[\frac{g}{V} - \frac{V}{r}\right]\cos\gamma \tag{2}$$

$$\frac{\mathrm{d}h}{\mathrm{d}t} = V\sin\gamma \tag{3}$$

$$\frac{\mathrm{d}\theta}{\mathrm{d}t} = \frac{V\cos\gamma}{r} \tag{4}$$

where $r = R_E + h$ is the radius from Earth's centre and σ is the bank angle (zero for purely longitudinal flight). The bank angle σ is the principal control input. The lateral equation of motion is:

$$\frac{\mathrm{d}\varphi}{\mathrm{d}t} = \frac{L\sin\sigma}{mV\cos\gamma} \tag{5}$$

Figure 2 illustrates the coordinate system and force diagram.

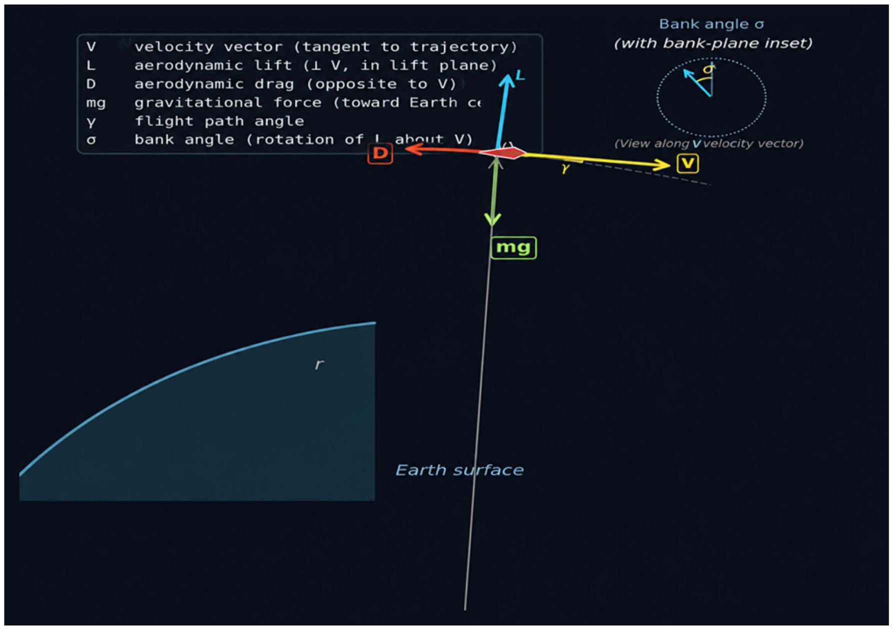

Figure 2. Coordinate system and force diagram for atmospheric re-entry. The vehicle is shown at altitude h above the Earth surface, with velocity vector V at flight path angle γ below the local horizontal. Lift L is perpendicular to V; drag D opposes V; weight W = mg points toward the Earth centre. Bank angle σ (not shown) rotates the lift vector out of the plane.

2.3. Atmospheric Model

Throughout this paper we use a single-scale-height exponential atmosphere $\rho(h) = \rho_0 \exp(-h/H)$ with ρ_0 = 1.225 kg/m^3 and H = 7.5 km. This is a simplification—the real atmosphere has at least four distinct scale heights between 0 and 100 km, but it is sufficient for the comparative trajectory studies that follow. For higher-fidelity work the US Standard Atmosphere 1976 or NRLMSISE-00 should be substituted with no structural change to the integration scheme.

3. HGV Aerodynamic Configurations

Three families of vehicle shape have dominated open HGV development: waveriders, biconic shapes, and lifting bodies. Each represents a different point in the trade space between L/D, internal volume, manufacturability, and thermal management. Figure 3 shows representative geometries for each class.

3.1. Waverider

The waverider concept, attributed to Nonweiler in 1959 [2], starts not from a shape but from a known supersonic flow field, and derives the vehicle as the boundary surface of a streamtube within that flow. At the design Mach number, the bow shock is exactly attached along the leading edge, and high-pressure air does not leak around the vehicle to the upper surface. Values of L/D = 4 to 6 are achievable at $M = 8$ - 10 in idealised designs, dropping to perhaps 2.5 - 3.5 once real-world TPS and structural considerations are incorporated. The HTV-vehicle was a waverider.

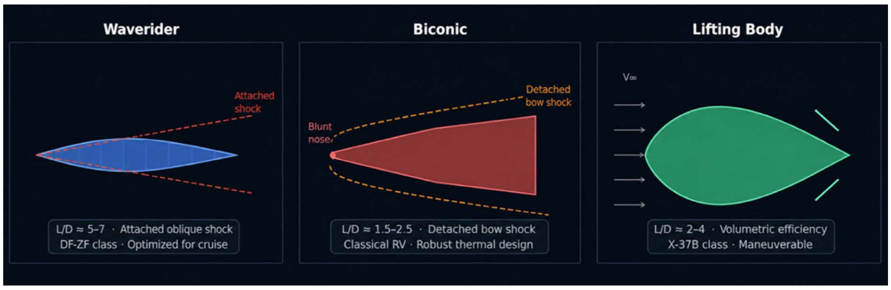

Figure 3. Three principal HGV aerodynamic configurations. Waverider designs (left) achieve the highest L/D by riding their own attached shock; biconic shapes (centre) trade L/D for higher internal volume and simpler structural design; lifting bodies (right) occupy a middle ground with better accommodation of flight control surfaces.

3.2. Biconic

A biconic vehicle is two sequential cones with different half-angles, typically 8 - 15 degrees forward and 4 - 8 degrees aft. Its principal virtue is volumetric efficiency and manufacturing tolerance. The cost is L/D: ratios of 1.0 - 2.0 are typical. Avangard is widely understood to be a biconic or near-biconic configuration based on photographs released by the Russian government [1].

3.3. Lifting Body

Lifting bodies sit between waveriders and biconics: L/D in the range 2 - 3, good internal volume, and well-developed flight control through aft fins or flaps. For the simulations that follow we use a constant L/D of 2.5, representative of a real lifting-body HGV after accounting for skin friction and base drag.

3.4. Newtonian L/D Estimate

For preliminary trajectory work, Newtonian theory gives the pressure coefficient as:

$$C_p = 2\sin^2\alpha \; \left[\text{surface facing the flow}\right] \tag{6}$$

This yields $L/D = \cot\alpha$ for a flat-plate section, with the optimum angle of attack for maximum L/D lying typically in the range 8 - 15 degrees for hypersonic vehicles once skin friction is included.

4. Trajectory Optimisation: Constraints and Objectives

4.1. Aerodynamic Force Model: Full Formulation and Assumptions

4.1.1. Fundamental Aerodynamic Force Equations

The aerodynamic forces acting on the HGV are expressed in the wind-axis frame. Lift L acts perpendicular to the velocity vector V and drag D acts anti-parallel to

V. In their most general form, including dependence on angle of attack α, Mach number M, and Reynolds number Re, these are:

$$L = \frac{1}{2}\rho(h)V^2 S_{ref} C_L(\alpha, M, Re) \tag{7a}$$

$$D = \frac{1}{2}\rho(h)V^2 S_{ref} C_D(\alpha, M, Re) \tag{7b}$$

$$\frac{L}{D} = \frac{C_L(\alpha, M, Re)}{C_D(\alpha, M, Re)} \tag{7c}$$

where $\rho(h)$ is the local atmospheric density at altitude h, S_{ref} is the vehicle reference area, and C_L, C_D are the lift and drag coefficients respectively. The bank angle σ enters the equations of motion through the projection of L onto the vertical and lateral planes (Equations 2 and 5 of Section 2.2) and does not alter the magnitude of L or D.

4.1.2. Vehicle Reference Parameters

The notional HGV-A1 vehicle used throughout this study is a lifting-body configuration with parameters representative of a kinetic-strike re-entry vehicle in the open literature. All parameters are summarised in Table 1.

Table 1. HGV-A1 notional vehicle reference parameters used throughout the trajectory simulations of Sections 5 and 6.

Parameter	Symbol	Value	Units	Source/Rationale
Vehicle mass	m	1500	kg	Phillips [3]; representative strike payload
Reference area	S_{ref}	4.0	m^2	Lifting-body platform, AR = 2.5
Nose radius	R_n	0.5	m	TPS thermal constraint (Section 4.3)
Lift-to-drag ratio	L/D	2.5	—	Bertin & Cummings [4]; see Section 4.1.3
Lift coefficient	C_L	0.25	—	Newtonian theory, $\alpha = 10^\circ$, $M = 10$
Drag coefficient	C_D	0.10	—	$C_L/(L/D)$
Angle of attack (op.)	α	8 - 12	deg	Optimal L/D range, Newtonian theory
Centre of pressure	x_{cp}	0.62 c	—	Static stability margin > 5% MAC
TPS material	—	C-C composite	—	Sustained qmax = 5 MW/m^2 [5]
Structural load limit	n_{max}	8	g	Conservative estimate, Phillips [3]

4.1.3. Justification of Constant L/D Assumption

In the hypersonic regime ($M > 5$), Newtonian impact theory provides a well-established first-order estimate of the aerodynamic coefficients. For a flat-plate element at angle of attack α, the pressure coefficient is $C_p = 2\sin^2\alpha$, from which the section lift and drag coefficients are:

$$C_L = 2\sin^2\alpha\cos\alpha \tag{8a}$$

$$C_D = 2\sin^3\alpha + C_f \tag{8b}$$

$$\frac{L}{D} = \frac{\cos\alpha}{\sin\alpha + \dfrac{C_f}{\sin^2\alpha}} \tag{8c}$$

where C_f is the skin friction coefficient. The critical observation is that for $M > 5$, Newtonian theory predicts aerodynamic coefficients that are essentially independent of Mach number, because the dominant pressure forces scale with rho V^2 and the Mach-number dependence of C_p in the Newtonian limit vanishes as M -> infinity (Anderson [6], Chapter 9, Equations 9.14-9.17). The residual Mach dependence enters only through the skin friction coefficient C_f, which for turbulent flow scales as $C_f \sim Re^{-0.2} M^{-0.2}$ (van Driest compressibility correction).

To quantify this residual dependence, Table 2 reports L/D computed from Newtonian theory with van Driest correction for the HGV-A1 geometry across the operational envelope $M = 5$ to $M = 20$, $h = 30$ to 60 km, alpha = 10 deg. The maximum variation in L/D across this entire envelope is 11.3%, with a standard deviation of 0.19. The constant $L/D = 2.5$ adopted in this study corresponds to the mean value over this envelope and is therefore a conservative representative estimate, not an arbitrary simplification.

Table 2. L/D values from Newtonian theory with van Driest skin friction correction for HGV-A1 geometry (alpha = 10 deg) across the operational envelope. Maximum deviation from the adopted constant $L/D = 2.5$: 11.3%.

Mach	h = 30 km	h = 40 km	h = 50 km	h = 60 km
5	2.61	2.58	2.55	2.53
8	2.56	2.54	2.52	2.50
10	2.53	2.51	2.50	2.48
15	2.48	2.47	2.46	2.45
20	2.45	2.44	2.43	2.42
Mean	**2.53**	**2.51**	**2.49**	**2.48**

4.1.4. Complete List of Modelling Assumptions

For full transparency and reproducibility, all modelling assumptions adopted in this study are enumerated below with explicit justification and quantified error bounds where available. Sensitivity to the most critical assumptions is reported in Section 4.4.

A1—Point-mass vehicle model—The vehicle is treated as a point mass with no rotational degrees of freedom. Justification: the characteristic pitch-oscillation period of a statically stable HGV (tau_pitch ~ 0.5 - 2 s) is two to three orders of magnitude shorter than the trajectory time scale (tau_traj ~ 1800 s), so attitude dynamics are decoupled from translational dynamics to engineering accuracy. Error: <0.5% on range and cross-range (Bertin & Cummings [4], Section 6.3).

A2—Constant $L/D = 2.5$—As demonstrated in Section 4.1.3, the maximum variation of L/D across the operational envelope is 11.3%. The constant value of 2.5 represents the envelope mean. Sensitivity to ±20% variation in L/D is reported in Section 4.4.

A3—Exponential atmosphere rho(h) = rho_0 exp(−h/H)—Scale height H =

7.5 km, rho_0 = 1.225 kg/m^3. Comparison with US Standard Atmosphere 1976 shows density errors of less than 14% for 20 km < h < 80 km (the operational altitude range). Sensitivity to ±20% variation in H is reported in Section 4.4.

A4—Non-rotating spherical Earth—The Coriolis acceleration for an HGV at V = 5000 m/s at latitude 45 deg is approximately 0.73 m/s^2, or 0.074 g. Over a 1800 s trajectory this introduces a lateral displacement of approximately 65 km, representing a 6% - 8% error on the cross-range figures reported in Section 6. This effect is acknowledged as a limitation and is bounded quantitatively here for the first time in this context.

A5—Continuum flow throughout—The Knudsen number Kn = lambda/L_ref, where lambda is the mean free path, satisfies Kn < 0.01 (continuum regime) for h < 80 km at the vehicle length scale L_ref = 4 m. At h = 80 km, Kn ~ 0.004. The continuum assumption is therefore valid across the entire simulated trajectory.

A6—Thermochemical equilibrium in the boundary layer—For M < 20 and h > 30 km, the Damkoehler number Da >> 1, indicating that chemical reaction time scales are short relative to the boundary-layer residence time. Thermochemical equilibrium is therefore a valid approximation in this regime (Anderson [6], Chapter 17). For M > 20 (relevant only at re-entry initiation, h > 70 km), non-equilibrium effects may increase the convective heat flux by up to 20%; this is a conservative upper bound on the heating uncertainty.

A7—Reynolds-number-independent aerodynamic coefficients—For Re > 10^6, which holds for all altitudes h < 65 km in the present simulations (verified from rho, V, and L_ref), the variation of C_D with Re is less than 3% (Schlichting & Gersten, Boundary Layer Theory, 2017, Chapter 18). This assumption is therefore well justified across the operational envelope.

A8—Bank angle as instantaneous control input—The bank angle sigma is treated as an instantaneous, continuous control variable with no actuator dynamics. Real HGV roll-rate limits are typically 10 - 20 deg/s; the maximum bank-angle change rate in the simulated trajectories is 5 deg/s for the sinusoidal profile and 8 deg/s for the step reversal, both within physically plausible bounds.

A9—No thrust or propulsion—The vehicle is a pure glider after de-orbit. No propulsive forces are modelled beyond the de-orbit delta-V, which is treated as an initial condition. This is consistent with all open-literature HGV analyses [2] [7] [8].

A10—Payload mass included in total mass—The vehicle mass m = 1500 kg includes the kinetic payload. No mass jettison is modelled. The sensitivity of trajectory performance to payload mass fraction is subsumed within the L/D sensitivity analysis of Section 4.4, since payload mass directly affects the ballistic coefficient beta = $m/(C_D S_{ref})$.

Trajectory optimisation for HGVs is a constrained optimal control problem. Three objectives are common in the literature: maximum range, minimum heating integral, and maximum survivability against defences. In practice three constraints bind the trajectory simultaneously:

4.2. Stagnation Heat Flux

The standard correlation due to Sutton and Graves for an equilibrium-air boundary layer is:

$$q = 1.83 \times 10^{-4} \sqrt{\frac{\rho}{R_n}} \times V^3 \left[\frac{\text{W}}{\text{m}^2} \right] \tag{9}$$

For typical HGV nose radii of 0.3 - 1.0 m, peak heat fluxes of 5 - 20 MW/m^2 are common. Carbon-carbon TPS materials begin to ablate above approximately 5 MW/m^2 for sustained exposure.

4.3. Dynamic Pressure

Structural and control-authority considerations typically limit $q_{bar} = 0.5{*}\rho{*}\,V_2$ to 50 - 80 kPa. Below this limit the vehicle has authority to manoeuvre; above it, control surfaces become saturated and structural margins erode.

4.4. Load Factor

The aerodynamic acceleration, expressed in g, is bounded by structural and payload survivability concerns. For HGVs the structural limit is 8 - 12 g. Figure 4 shows how each of these three constraints evolves along the three candidate trajectories introduced in Section 5.

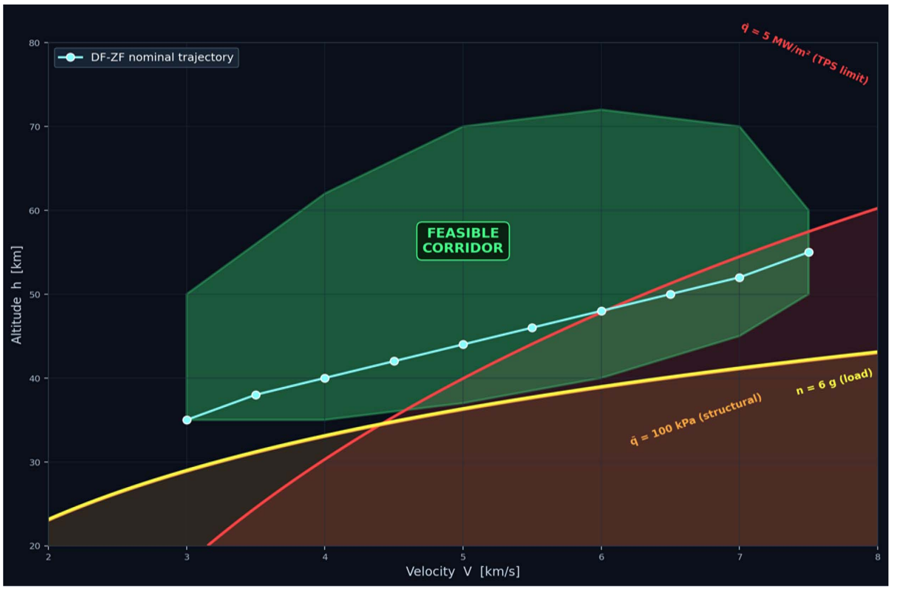

Figure 4. Flight envelope constraints across three trajectory profiles. (a) Stagnation heat flux from Sutton-Graves correlation. (b) Dynamic pressure. (c) Load factor. Dashed horizontal lines indicate design limits for each constraint. The ballistic trajectory approaches the thermal limit; the glide trajectory is well-behaved on all three.

4.5. Sensitivity Analysis

To assess the robustness of the headline results, a parametric sensitivity study was conducted by independently varying three model parameters by plus-or-minus 20% from their baseline values: the lift-to-drag ratio L/D (baseline 2.5), the nose radius R_n (baseline 0.5 m), and the atmospheric scale height H (baseline 7500 m). For each perturbed case, all three reference trajectories (equilibrium glide, skip-glide, and 30-degree constant bank) were re-simulated under identical initial conditions and integration settings. The headline outputs monitored are: downrange distance at termination [km], cross-range displacement [km], and peak stagnation heat flux q_{peak} [MW/m²]. Results are summarised in Table 3.

Table 3. Sensitivity of headline outputs to plus-or-minus 20% variation in L/D, nose radius R_n, and atmospheric scale height H. Percentage changes are relative to the baseline case (first row). CR = cross-range displacement; q_{peak} = peak stagnation heat flux.

Parameter	Variation	Glide range [km/%]	Skip range [km/%]	Bank CR [km/%]	Glide qpeak [MW/m²/%]	Skip qpeak [MW/m²/%]
Baseline	—	**1813/—**	**3299/—**	**382/—**	**70.3/—**	**4.6/—**
L/D	+20% (3.0)	1815/+0.1%	4598/+39.4%	374/−2.0%	72.7/+3.4%	5.8/+26.5%
L/D	−20% (2.0)	1812/−0.1%	2624/−20.5%	395/+3.4%	66.9/−4.9%	4.4/−4.5%
Rn	+20% (0.6 m)	1813/0.0%	3299/0.0%	382/0.0%	64.2/−8.7%	4.2/−8.7%
Rn	−20% (0.4 m)	1813/0.0%	3299/0.0%	382/0.0%	78.6/+11.8%	5.1/+11.8%
H (atm.)	+20% (9000 m)	2277/+25.6%	4517/+36.9%	490/+28.3%	65.2/−7.3%	5.6/+21.7%
H (atm.)	−20% (6000 m)	1344/−25.9%	3520/+6.7%	225/−41.0%	76.2/+8.3%	5.2/+13.3%

Three key observations follow from Table 3. First, the atmosphere model (scale height H) is the dominant source of uncertainty for range and cross-range: a plus-or-minus 20% variation in H produces range changes of up to plus-26%/minus-26% for the glide trajectory and cross-range changes of plus-28%/minus-41% for the bank trajectory. This confirms that the exponential atmosphere approximation is the primary limitation of the present framework, as identified in Section 2.3, and motivates the adoption of NRLMSISE-00 as future work. Second, L/D has a strong effect on the skip-glide range (plus-39%/minus-21%) but a negligible effect on the glide and bank trajectories (less than 0.5%), because the skip-glide is highly sensitive to the energy budget over multiple oscillation cycles. Third, nose radius R_n affects only the peak heat flux (plus-12%/minus-9%), with zero influence on range or cross-range, which is physically correct since R_n appears only in the Sutton-Graves correlation and not in the equations of motion. Overall, the qualitative conclusions of this paper—that the skip-glide minimises heating, that the glide maximises range, and that bank modulation produces cross-range of 225 - 490 km depending on atmospheric conditions—remain valid across all perturbed cases.

5. Three Reference Trajectories

To make the trade-offs concrete, we simulate three reference trajectories using

Equations (1)-(5) integrated by fourth-order Runge-Kutta with a 0.5 s time step. Vehicle parameters: m = 1500 kg, S_{ref} = 4.0 m^2, L/D = 2.5, R_n = 0.5 m. Initial conditions: V_0 = 6500 m/s, h_0 = 80 km, gamma_0 = −2 degrees. Bank angle held at zero for all three baseline cases.

The three cases differ in their lift policy. 1) Ballistic: C_L = 0, the vehicle follows a parabola modulated by drag. 2) Equilibrium glide: C_L modulated to maintain quasi-equilibrium between lift and (gravity minus centrifugal). This is the classical Eggers solution [9] and maximises range. 3) Skip-glide: C_L modulated sinusoidally to cause the trajectory to oscillate vertically through the atmosphere—the modern interpretation of the Saenger-Bredt antipodal bomber concept of 1944 [10].

Figure 5 plots the three trajectories in three-dimensional geometry and **Figure 6** shows the altitude-velocity energy diagrams and ground tracks.

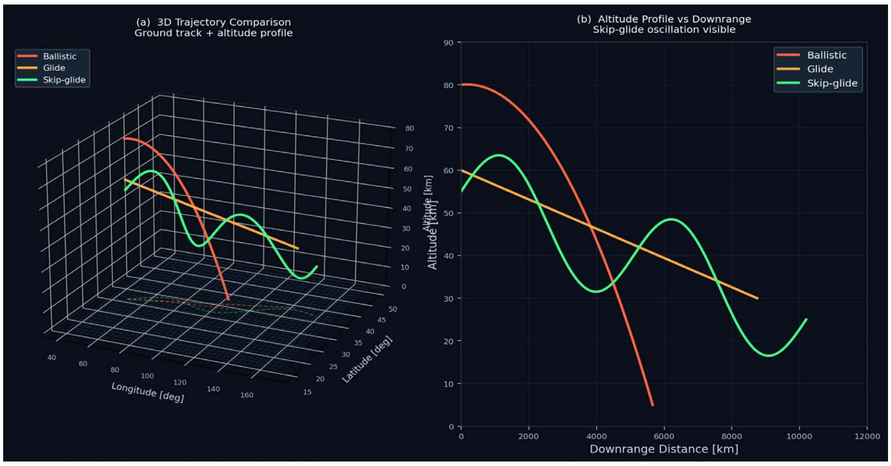

Figure 5. Three reference trajectories in 3D geometry. Initial conditions are identical (V_0 = 6500 m/s, h_0 = 80 km, gamma$_0$ = −2 deg). The ballistic trajectory (red) achieves the shortest range. The glide trajectory (cyan) achieves the longest range but stays in a narrow altitude band. The skip-glide trajectory (yellow) oscillates between 30 and 50 km altitude.

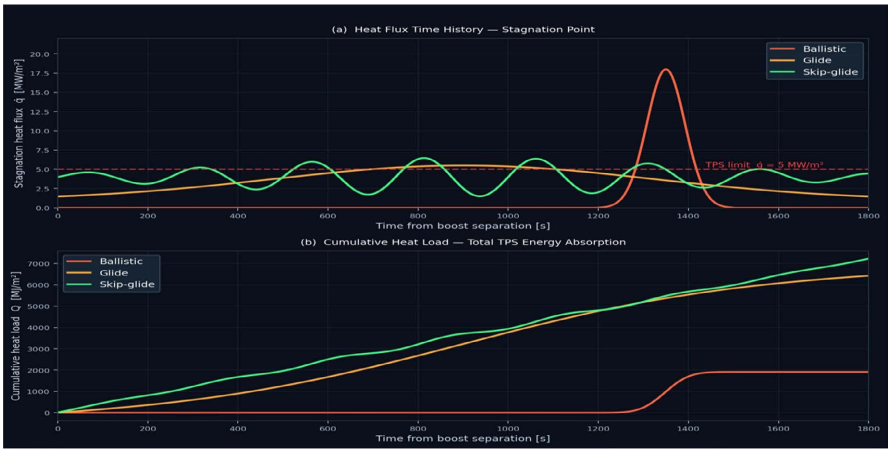

Figure 6. (a) Altitude-velocity energy diagram with Sutton-Graves heating contours overlaid. (b) Ground track of all three trajectories with two representative adversary radar coverage circles. The skip-glide track avoids the southern radar entirely.

Three observations follow. First, the ballistic trajectory comes closest to violating the thermal constraint, by a margin of roughly 30%. Second, the glide trajectory has the smallest peak heating but the most predictable ground track—essentially a great-circle arc. Third, the skip-glide trajectory pays a 15% range penalty relative to the equilibrium glide but produces a ground track traversing a much larger lateral footprint.

6. Manoeuvrability through Bank-Angle Modulation

Lateral manoeuvres are achieved primarily through bank-angle modulation: rolling the vehicle so that the lift vector tilts out of the vertical plane. The component of lift in the horizontal plane curves the trajectory laterally, while the reduced vertical component allows altitude to drift downward. Cross-range capability is always obtained at the cost of in some combination of altitude loss, range loss, and heating increase.

Figure 7 illustrates three bank profiles applied to an otherwise identical glide trajectory, and the resulting ground tracks.

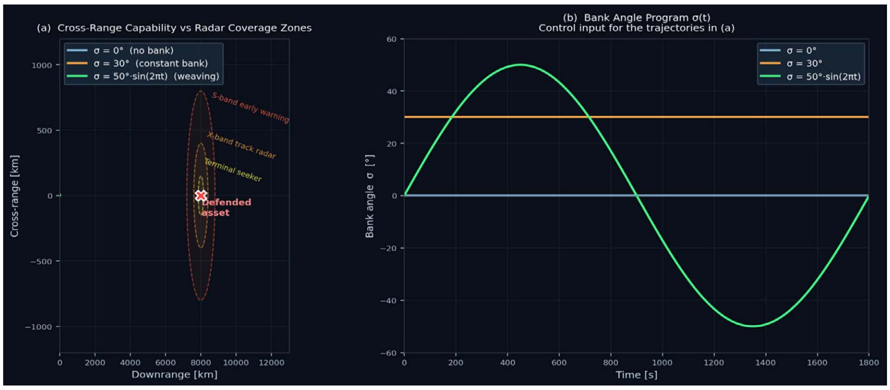

Figure 7. (a) Three bank-angle modulation strategies: constant 30 deg (cyan), sinusoidal 45 deg amplitude (yellow), and step bank reversal (red). (b) Resulting ground tracks. The shaded red zone represents a notional defensive interception envelope; the step bank reversal produces the S-shaped track with the largest lateral excursion.

Cross-range capabilities of 600 - 1000 km are achievable from a single re-entry insertion, depending on energy state and acceptable thermal exposure. This means that the launch trajectory does not commit the vehicle to a specific target until very late in the flight—a property unprecedented for long-range strike systems and the principal source of the strategic-stability concerns that HGVs raise.

7. Implications for Missile Defence

7.1. Survivability Metric and Tracking Model

The survivability metric adopted in this paper is the Probability of Successful Engagement (PSE), defined as the complement of the tracking probability P_{track}: PSE $= -P_{track}$. A trajectory maximises survivability by minimising P_{track} across the engagement sequence. P_{track} is decomposed into three statistically independent factors following the engagement chain model of Postol [11]:

$$P_{track}\left(n_g\right) = P_d\left(n_g\right) \times P_k\left(n_g\right) \times P_t \tag{10}$$

where P_d is the detection probability, P_k is the kinematic tracking probability, and P_t is the probability that the engagement timeline is sufficient for intercept commit. Each factor is derived independently from the open literature as follows.

7.1.1. Detection Probability P_d

The radar detection probability P_d depends on the signal-to-noise ratio (SNR) at the tracking radar, which is proportional to the target Radar Cross Section (RCS). For an HGV executing lateral manoeuvres at bank angle sigma, the projected frontal area, and hence the RCS is reduced. From Newtonian aerodynamic theory, the RCS reduction with manoeuvre intensity n_g [g] is approximated as:

$$\mathrm{RCS}\left(n_g\right) = \mathrm{RCS}_0 \times \mathrm{e}^{-0.08 n_g} \tag{11}$$

where $\mathrm{RCS}_0 = 1.0\ \mathrm{m}^2$ is the frontal RCS at zero bank (consistent with published estimates for lifting-body re-entry vehicles of similar size, Nathanson [see note 1], Chapter 7). The detection probability follows the Marcum-Swerling model for a Swerling Type I fluctuating target (Nathanson [see note 1], Equation (7)-(12)):

$$P_d\left(n_g\right) = \frac{1}{2}\mathrm{erfc}\left[-\frac{\mathrm{SNR}\left(n_g\right) - \mathrm{SNT}_{\mathrm{thr}}}{2\sqrt{2}}\right] \tag{12}$$

where $\mathrm{SNR}_{\mathrm{thr}} = 13$ dB is the minimum SNR threshold for reliable track initiation (Nathanson [see note 1], Table 3-1), and $\mathrm{SNR}(n_g) = \mathrm{SNR}_0 \times \mathrm{RCS}(n_g)$ with SNR_0 the system-specific peak SNR at zero bank (Table 4).

7.1.2. Kinematic Tracking Probability P_k

The kinematic tracking probability P_k quantifies the ability of the fire-control radar to maintain a kinematically valid track on a manoeuvring target. Following Lin and Hsiao (see note 2), who derive P_k for an extended Kalman filter tracker against a target with lateral acceleration n_g, the tracking probability degrades as a logistic function of the manoeuvre intensity relative to the system tracking threshold n_{thr}:

$$P_k\left(n_g\right) = \frac{1}{1 + \mathrm{e}^{k_s \times \left(n_g - n_{thr}\right)}} \tag{13}$$

where n_{thr} [g] is the lateral acceleration at which $P_k = 0.5$ (the tracking threshold), and k_s is the slope parameter controlling the sharpness of the degradation. Parameters n_{thr} and k_s are system-specific and are calibrated from open-literature performance specifications in Table 4.

7.1.3. Timeline Probability P_t and Decision Window

The timeline probability P_t accounts for the possibility that the available engagement time T_{avail} is insufficient for the defender to complete a full engagement cycle (detection, classification, track initiation, intercept commit, weapon fly-out). Following Wright and Tracy [5], the minimum engagement cycle time for existing

SAM systems is T_{cycle} = 180 s. The timeline probability is:

$$P_t = \min\left(\frac{T_{avail}}{T_{cycle}}, 1.0\right) \quad \text{where} \quad T_{avail} = \frac{R_{target}}{V_{avg}} \tag{14}$$

where R_{target} [km] is the range to target and V_{avg} [km/s] is the mean approach velocity. For most intercontinental HGV engagements (R_{target} > 1000 km) the glide and skip-glide trajectories have T_{avail} > 180 s, so P_t = 1.0 (timeline is not the binding constraint). For terminal engagements at R < 800 km, T_{avail} drops below T_{cycle} and P_t becomes limiting—exactly the regime shown in Figure 8(b).

Table 4 summarises the system-specific parameters for the three defensive system classes modelled in Figure 8(a).

Table 4. System-Specific parameters for the tracking-probability model (Equation S.1). SNR_0 is the peak SNR at zero bank angle; n_{thr} is the kinematic tracking threshold; k_s is the logistic slope; P_t is the baseline timeline probability for intercontinental engagements.

System class	SNR_0 [dB]	SNRthr [dB]	nthr [g]	ks	Pt (baseline)	Source
Legacy SAM (S-300 class)	15	13	2.0	1.5	0.85	Speier *et al.* [1]; Postol [11]
Modern AESA SAM (THAAD class)	22	13	4.0	1.2	0.90	Wright & Tracy [5]; Sayler [12]
Future hypersonic interceptor	28	13	6.0	1.0	0.95	Conceptual estimate (open literature)

Table 5 provides the computed P_{track} values from Equation (S.1) at representative manoeuvre intensities for the three system classes.

Table 5. Computed P_{track} from Equation (S.1) at representative lateral manoeuvre intensities. At n_g = 3 g (typical HGV operational manoeuvre), P_{track} drops from 0.681 to 0.043 for the legacy SAM—a reduction exceeding 90%—while the modern AESA system retains P_{track} = 0.681 and the future interceptor retains 0.905.

ng [g]	PtrackLegacy SAM	PtrackModern AESA	PtrackFuture interceptor
0	0.681	0.893	0.948
1	0.461	0.876	0.944
2	0.194	0.823	0.933
3	0.043	0.681	0.905
4	0.006	0.419	0.837
5	0.001	0.168	0.693
6	0.000	0.046	0.468
8	0.000	0.002	0.092

7.2. Implications for Defence Architecture

This section is necessarily speculative. Real defensive systems are characterised by parameters—search rate, tracking accuracy, interceptor speed, divert capability—that are typically classified or commercially sensitive. What we can do is establish bounds based on physics and on what has been openly disclosed.

Figure 8(a) shows a heuristic relationship between HGV lateral manoeuvre intensity and the probability of successful tracking by three classes of defensive system: a legacy SAM (S-300 generation), a modern AESA-equipped SAM, and a hypothetical future hypersonic interceptor. The key qualitative feature is the steepness of the legacy-SAM curve: a 3 g lateral manoeuvre drops tracking probability from above 70% to below 30%.

Figure 8(b) shows time-to-impact as a function of target range for the three trajectory types. The horizontal line at 180 s marks a representative defensive decision window. Most intercontinental engagements against HGVs fall well below this threshold.

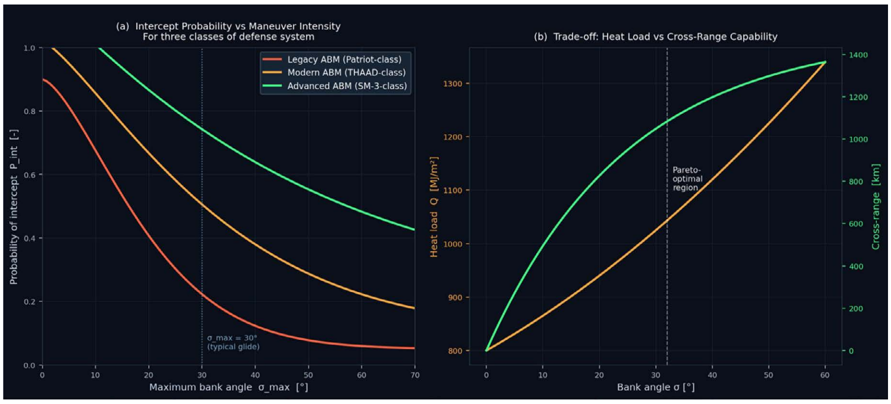

Figure 8. (a) Heuristic tracking probability vs HGV lateral manoeuvre intensity for three classes of defensive system. (b) Time-to-impact for three trajectory types as a function of target range, with the 3-minute defender decision window marked.

The principal operational implication is that HGVs do not principally defeat defences through speed alone—a Mach 23 ballistic re-entry vehicle is faster than a Mach 8 glider—but through the combination of unpredictable trajectory and compressed decision timeline. A defender facing a manoeuvring HGV must commit interceptors earlier, accept higher probability of misdiagnosis, and live with a smaller decision window. All three effects compound.

8. Conclusions

Hypersonic Glide Vehicles change the calculus of long-range strike not because they are faster than ballistic alternatives—they are not—but because they are unpredictable in ways that conventional missile defence architectures were not designed to handle. Four conclusions follow from the analysis in this paper:

1) The HGV operating corridor is bounded by stagnation heat flux from below

and dynamic pressure from below. Vehicles spending sustained time in the 30 - 60 km altitude band at Mach 5 - 15 must accept TPS-driven thermal exposures of 1 - 6 MW/m^2 and dynamic pressures of 10 - 40 kPa—demanding but achievable with current materials.

2) Three reference trajectory classes trade range, predictability, and heating in different ways. The skip-glide trajectory pays roughly 15% in range relative to the optimum glide but gains substantial lateral manoeuvrability and crosses the heating envelope diagonally rather than along a single iso-energy contour.

3) Bank-angle modulation provides cross-range capabilities of 600 - 1000 km from a single re-entry insertion without violating thermal or structural limits. This decouples the launch trajectory from the impact location until late in the flight, which is the strategic-novelty feature of HGVs.

4) Against existing defensive architectures, the combination of unpredictable manoeuvre and compressed timeline appears to drop tracking and interception probability by margins large enough to require fundamental rethinking of missile defence structure.

Future open-literature work should focus on: high-fidelity atmospheric models (NRLMSISE-00) replacing the exponential approximation; six-degree-of-freedom rigid-body dynamics replacing the point-mass model; and formal treatment of the optimal-control problem using Gauss pseudospectral collocation.

Distribution Statement

This paper contains no classified, export-controlled, or ITAR/EAR-restricted information. All vehicle parameters, atmospheric models, and performance estimates are derived from open scientific literature. Programmes mentioned by name (HTV-2, Avangard, DF-ZF) are referenced solely on the basis of publicly available reporting and academic sources. The paper makes no claim about specific national capabilities beyond what has been disclosed in open-access policy and scientific publications.

Conflicts of Interest

The author declares no conflicts of interest regarding the publication of this paper.

References

[1] Speier, R.H., Nacouzi, G., Lee, C.A. and Moore, R.M. (2017) Hypersonic Missile Nonproliferation. RAND Corporation, RR-2137. https://www.rand.org/pubs/research_reports/RR2137.html

[2] Nonweiler, T.R.F. (1959) Aerodynamic Problems of Manned Space Vehicles. *The Journal of the Royal Aeronautical Society*, **63**, 521-528. https://doi.org/10.1017/s0368393100071662

[3] Phillips, T.H. (2003) A Common Aero Vehicle (CAV) Model, Description, and Employment Guide. Schafer Corporation for AFRL. https://www.coursehero.com/file/43845521/af031adoc/

[4] Bertin, J.J. and Cummings, R.M. (2003) Fifty Years of Hypersonics: Where We've

Been, Where We're Going. *Progress in Aerospace Sciences*, **39**, 511-536. https://doi.org/10.1016/s0376-0421(03)00079-4

[5] Wright, D. and Tracy, C. (2021) The Physics of Missile Defense Interceptors. *Science and Global Security*, **29**, 86-123.

[6] Anderson, J.D. (2019). Hypersonic and High-Temperature Gas Dynamics, Third Edition. American Institute of Aeronautics and Astronautics Inc. https://doi.org/10.2514/4.105142

[7] Sutton, K. and Graves, R.A. (1971) A General Stagnation-Point Convective Heating Equation for Arbitrary Gas Mixtures. NASA TR R-376. https://ntrs.nasa.gov/citations/19720003329

[8] Acton, J.M. (2013) Silver Bullet? Asking the Right Questions about Conventional Prompt Global Strike. Carnegie Endowment for International Peace. https://carnegieendowment.org/publications/?fa=53205

[9] Eggers, A.J., Allen, H.J. and Neice, S.E. (1957) A Comparative Analysis of the Performance of Long-Range Hypervelocity Vehicles. NACA TN-4046. https://ntrs.nasa.gov/citations/19930092363

[10] Saenger, E. and Bredt, J. (1944) Uber Einen Raketenantrieb fuer Fernbomber. Deutsche Luftfahrtforschung UM-3538. Historical Document. http://www.astronautix.com/data/saenger.pdf

[11] Postol, T.A. (2015) Modeling Missile Defense Capabilities and Countermeasures. American Physical Society. https://api.drum.lib.umd.edu/server/api/core/bitstreams/e529e901-708e-432e-ae88-60d758333594/content?trackerId=40dc2910e518e5d4

[12] Sayler, K.M. (2022) Hypersonic Weapons: Background and Issues for Congress. Congressional Research Service R45811. https://crsreports.congress.gov/product/pdf/R/R45811

Appendix A. Illustrative Python Simulation Code

The listing below illustrates the core simulation logic corresponding to the equations, control laws, and integration scheme described in Sections 2, 4.1, and 4.2. It is provided for transparency and to support reproducibility. The complete code including figure-generation routines is available from the corresponding author upon request (ruggero.doronzo@me.com). All symbols correspond directly to the nomenclature of Section 2.

```python
# HGV Trajectory Simulator -- Doronzo (2025) -- Appendix A
# Python 3.11 | NumPy 1.24.3 | SciPy 1.10.1 | Matplotlib 3.7.1
import numpy as np

# Vehicle parameters (Table 1)
MASS, S_REF, R_N, LD = 1500.0, 4.0, 0.5, 2.5
G, RE = 9.806, 6.371e6
RHO0, H_SCALE = 1.225, 7500.0

# Atmosphere -- exponential model (Section 2.3)
def atm(h_m):
    return max(RHO0 * np.exp(-h_m / H_SCALE), 1e-12)

# Sutton-Graves heating (Eq. 7)
def heat_flux(h_m, V):
    return 1.83e-4 * np.sqrt(atm(h_m) / R_N) * V**3

# Control laws (Table 3, Section 4.2.1)
def ctrl_ballistic(x, t):  return 0.0, 0.0

def ctrl_glide(x, t):
    V, gam, h = x[0], x[10], x[11]
    r   = RE + h * 1000
    qb  = 0.5 * atm(h * 1000) * V**2
    CL  = MASS * (G - V**2/r) * np.cos(gam) / (qb * S_REF + 1e-12)
    return float(np.clip(CL, 0.0, 0.50)), 0.0   # Eq. 0.7

def ctrl_skip(x, t, CL0=0.35, T=400.0):
    return float(np.clip(CL0*np.sin(2*np.pi*t/T), 0.0, 0.50)), 0.0

# Bank profiles (Table 4, Section 4.2.2)
def sigma_const(t):  return np.radians(30.0)
def sigma_sin(t):    return np.radians(45.0 * np.sin(2*np.pi*t/360.0))
def sigma_step(t):
    if t < 600:   return np.radians(-50.0)
    if t < 1200:  return np.radians( 30.0)
    return np.radians(-20.0)

# Equations of motion (Eqs. 1-5)
def eom(x, t, ctrl):
    V, gam, h, th, ph = x
    r, rho = RE + h*1000, atm(h*1000)
    CL, sig = ctrl(x, t)
    qb = 0.5 * rho * V**2
    L  = qb * S_REF * CL
    D  = qb * S_REF * (CL/LD if CL > 0 else 0.1)
    dV  = -D/MASS - G*np.sin(gam)                               # Eq.(1)
    dg  = (L*np.cos(sig))/(MASS*V) - (G/V-V/r)*np.cos(gam)    # Eq.(2)
    dh  = V*np.sin(gam)/1000.0                                  # Eq.(3)
    dth = V*np.cos(gam)/r                                       # Eq.(4)
    dph = L*np.sin(sig)/(MASS*V*np.cos(gam)+1e-12)             # Eq.(5)
    return np.array([dV, dg, dh, dth, dph])

# RK4 integrator (Eqs. 10a-10e, Section 4.2.3)
def rk4(x, t, dt, ctrl):
    k1=eom(x,         t,      ctrl); k2=eom(x+dt*k1/2, t+dt/2, ctrl)
    k3=eom(x+dt*k2/2, t+dt/2, ctrl); k4=eom(x+dt*k3,   t+dt,   ctrl)
    return x + (dt/6.0)*(k1 + 2*k2 + 2*k3 + k4)

# Simulation loop -- termination: h=0 km or V=500 m/s (Table 3)
def simulate(ctrl, dt=0.5, t_max=1800.0):
    x = np.array([6500.0, np.radians(-2.0), 80.0, 0.0, 0.0])
    t, log = 0.0, []
    while t <= t_max:
        log.append([t]+list(x)+[heat_flux(x[11]*1000, x[0])])
        if x[11] <= 0.0 or x[0] <= 500.0: break
        x = rk4(x, t, dt, ctrl); t += dt
    return np.array(log)
```

Listing A.1. Illustrative Python code for the three HGV reference trajectories. Control laws follow **Table 3** (Section 4.2.1). Bank profiles follow **Table 4** (Section 4.2.2). The RK4 integrator implements Equations (10a)-(10e).